ASME Journal of Engineering for Gas Turbines and Power
Online journal at:
https://asmedigitalcollection.asme.org/gasturbinespower

Michael Palman
Turbomachinery and Heat Transfer Laboratory,
Aerospace Engineering Department,
Technion – Israel Institute of Technology,
Haifa 3200003, Israel
e-mail: p.michael@campus.technion.ac.il

Anton Agapovichev
Turbomachinery and Heat Transfer Laboratory,
Aerospace Engineering Department,
Technion – Israel Institute of Technology,
Haifa 3200003, Israel
e-mail: antona@technion.ac.il

Yohai Abraham
Turbomachinery and Heat Transfer Laboratory,
Aerospace Engineering Department,
Technion – Israel Institute of Technology,
Haifa 3200003, Israel
e-mail: yohai.a@technion.ac.il

Vladimir Erenburg
Turbomachinery and Heat Transfer Laboratory,
Aerospace Engineering Department,
Technion – Israel Institute of Technology,
Haifa 3200003, Israel
e-mail: eren@technion.ac.il

Ahmet Yildirim
Turbomachinery and Heat Transfer Laboratory,
Aerospace Engineering Department,
Technion – Israel Institute of Technology,
Haifa 3200003, Israel
e-mail: ahmety@campus.technion.ac.il

Sercan Acarer
Associate Professor
Mechanical Engineering Department,
Izmir Katip Celebi University,
Izmir 35620, Turkey
e-mail: sercan.acarer@ikc.edu.tr

Arnaud Chatel
Turbomachinery Department,
von Karman Institute of Fluid Dynamics,
Waterloosesteenweg 72 B-1640,
Sint-Genesius-Rode, Belgium
e-mail: arnaud.chatel@vki.ac.be

Victor Loir
Turbomachinery Department,
von Karman Institute of Fluid Dynamics,
Waterloosesteenweg 72 B-1640,
Sint-Genesius-Rode, Belgium
e-mail: victor.loir@vki.ac.be

Design-for-Additive-Manufacturing Approach for Support-Free Pre-Assembled Micro Gas Turbines

This study presents a preliminary design approach for pre-assembled microgas turbine engines for unmanned aerospace propulsion systems, intended for fabrication via direct metal laser sintering, and demonstrates the feasibility of additively manufacturing nested, self-supporting turbomachinery systems from Inconel 718 in their operational configuration. The layout consists of two primary components: a monolithic rotor integrating the compressor and turbine, connected by a shaft that functions as a hybrid journal bearing lubricated by the engine's liquid fuel prior to combustion, and a stationary casing that incorporates turbomachinery stators, a bearing housing, and a porous inert media combustor. Each component is designed to be self-supporting within powder bed fusion constraints and to facilitate the build of connected geometries above it, enabling the entire engine to be formed in a single uninterrupted process. Using a multidisciplinary gradient-based optimization framework, the radial compressor and mixed-flow turbine are parametrically designed to maximize mass flow and aerodynamic efficiency while maintaining structural integrity. The porous inert media combustor comprising isotruss lattices achieves prevaporized lean premixed combustion with minimal pressure drop. A fluidic conical hybrid bearing is considered with effective surface scaling, providing sufficient axial/radial load capacity at reduced power requirements. To ensure printability, precompensation optimization mitigates residual process stress-induced deformations, resulting in a pre-assembled architecture with manufacturing deviations of 70 μm and surface roughness of 3 μm for all critical surfaces. This work demonstrates a scalable, system-level additive manufacturing (AM) approach that eliminates postassembly and significantly simplifies the production of complex turbomachinery, offering a practical pathway toward integrated AM-driven propulsion systems. [DOI: 10.1115/1.4069915]

Keywords: additive manufacturing, direct metal laser sintering, microgas turbines, pre-assembled turbomachinery, hybrid bearings, multidisciplinary optimization, radial compressor and mixed-flow turbine, aero-mechanical design, parametric design analysis, single print manufacturing, self-supporting structures, innovative propulsion systems

[1]Corresponding author.
Manuscript received June 8, 2025; final manuscript received September 11, 2025; published online December 4, 2025. Assoc. Editor: Ward De Paepe.

Tom Verstraete
Professor
Turbomachinery Department,
von Karman Institute of Fluid Dynamics,
Waterloosesteenweg 72 B-1640,
Sint-Genesius-Rode, Belgium
e-mail: tom.verstraete@vki.ac.be

Bayindir Huseyin Saracoglu
von Karman Institute of Fluid Dynamics,
AIAA Associate Fellow,
von Karman Institute of Fluid Dynamics,
Waterloosesteenweg 72 B-1640,
Sint-Genesius-Rode, Belgium
e-mail: bayindir.saracoglu@vki.ac.be

Beni Cukurel[1]
Associate Professor
Turbomachinery and Heat Transfer Laboratory,
Aerospace Engineering Department,
Technion – Israel Institute of Technology,
Haifa 3200003, Israel
e-mail: beni@cukurel.org

Introduction

The demand for microjet engines is rapidly increasing due to their growing applications in aerospace, unmanned aerial vehicles, and propulsion systems. The global market is projected to reach USD 3.55 billion in 2024, with an expected compound annual growth rate of 11.3% from 2024 to 2029, reaching USD 5.41 billion by 2030 [1,2]. However, high manufacturing costs, technical complexities, and supply chain disruptions—aggravated by global challenges such as pandemics and geopolitical instability—pose significant hurdles [3]. The traditional manufacturing of jet engines involves a complex and labor-intensive chain of operations. Turbines are typically cast, compressor impellers require precision computer numerical control milling, rotor shafts are turned, and combustor and casing assemblies involve sheet metal processing and welding. This intricate production chain relies on precise timing and coordination across multiple contractors. Any delay or deviation can disrupt the entire process, resulting in high production costs. Furthermore, the reliance on specialized processes and skilled labor adds to the overall expense, underscoring the need for more streamlined and cost-effective manufacturing solutions.

To address these challenges, the aerospace industry is increasingly adopting additive manufacturing (AM), which offers cost reduction, streamlined production, and enhanced design flexibility [4–6]. Among AM technologies, direct metal laser sintering (DMLS), a form of laser powder bed fusion (L-PBF), is particularly well-suited for producing complex metal components. In DMLS, a thin layer of fine metal powder, typically 20–60 μm thick, is evenly spread across a build platform. A high-intensity laser selectively melts the powder according to a sliced computer aided design (CAD) model, forming a dense, solid structure through rapid melting and solidification. After each layer is completed, the build platform lowers, and a recoater applies a fresh powder layer. This process is repeated iteratively until the entire component is formed. The build chamber is filled with inert gas, such as argon or nitrogen, to prevent oxidation and maintain material integrity. DMLS excels in fabricating intricate geometries with superior mechanical properties, making it highly suitable for aerospace applications requiring high precision and structural complexity [7–10]. Modern DMLS machines now feature build volumes of up to 400 mm and laser power reaching 1 kW, enabling the production of larger components. Research has shown that DMLS significantly streamlines production, consolidating multiple parts into fewer components, thereby reducing manufacturing costs and assembly time.

One notable example is General Electric's (GE) aviation division leveraging AM for jet engine production by integrating additively manufactured combustor fuel nozzles into its leading-edge aviation propulsion (LEAP) engines. These nozzles reduced the number of brazes and welds from 25 to five, leading to a 25% reduction in nozzle weight [11]. As of 2021, GE reported producing over 100,000 such nozzles, demonstrating the scalability of AM for high-volume aerospace applications. The Federal Aviation Administration certified the GE9X engine in 2020, which incorporates over 300 additively manufactured components [12]. This achievement highlights the potential for AM to meet stringent regulatory standards while maintaining quality and performance.

Other manufacturers are similarly advancing the use of AM in propulsion systems. Rolls-Royce is employing AM in the development of its Advance 3 engine, focusing on reducing part count and improving performance [13]. Siemens has leveraged AM to produce turbine blades for power generation [14], while Pratt & Whitney is using AM components in maintenance, repair, and overhaul applications [15]. Sierra Turbines further demonstrated the potential of AM for a microturbine by consolidating 61 separate parts that constituted the combustor, casing, shaft tunnel, and turbine stator into a single piece, significantly simplifying assembly and reducing production costs [16].

In the microjet engine market, fully additively manufactured engines have been developed as proof of concept. One early example is the microjet engine produced by Monash University, which showcased the feasibility of AM in aerospace propulsion during its unveiling at the Avalon International Airshow in 2015 [17]. GE also developed a laboratory-scale microgas turbine in 2018, which achieved 33,000 RPM in testing, demonstrating AM's capability to produce operationally viable engine components [18]. More recently, research has focused on evolving AM-based designs into mature propulsion systems with practical applications. Pratt and Whitney's Gator Works division is re-engineering the TJ-150 turbine to be entirely 3D-printed. The TJ-150, with a thrust rating of 667 N, is used in various military applications, including unmanned systems and missile propulsion [19]. Similarly, the Russian Scientific-Research Institute of Aviation Materials developed the

MGTD-20 engine, a 220 N thrust microgas turbine manufactured through AM. The MGTD-20 has undergone successful flight testing on unmanned aerial vehicles, further validating the applicability of AM in operational environments [20].

These efforts underline the growing maturity of AM technologies for aerospace propulsion systems, addressing challenges related to manufacturing complexity, part consolidation, and production efficiency. Current approaches primarily focus on component-level design, where individual parts—such as the combustor shell, compressor stator, turbine stator, and shaft—are designed for AM, and fabricated separately. However, these architectures still require significant postprocessing of components and elaborate multistep assembly. The next natural step in technological progression is to move beyond component-level optimization toward system-level coupling of design and manufacturing.

Motivation. The proposed research addresses this technological gap by advancing the pre-assembled turbomachinery design paradigm for microgas turbines, leveraging AM to its fullest potential. The presented architecture reduces the system to two main components: a rotating shaft (comprising a compressor and turbine) supported by a single hydrostatic bearing, and a stationary casing with an integrated combustion chamber. Designing self-supporting components that can be nested and printed in their operational configuration, enables the manufacture of an entire pre-assembled system in a single uninterrupted production sequence, eliminating the need for significant postprocessing steps.

Some of the foundational concepts for this research have already been independently validated by the coauthors. The ultramicrogas turbine tests demonstrated the feasibility of additively manufactured monolithic rotors, combining a compressor, turbine, and generator shaft into a single Inconel part [21–24]. Building on this, the turbocharger-based medical emergency ventilators project introduced pre-assembled turbomachinery systems with air-driven hydrostatic bearings, where both the rotor and the stationary housing were manufactured simultaneously from thermoplastic in a single fused deposition modeling process [25]. Building on these advancements, this paper focuses on evaluating the feasibility assessment of additively manufactured pre-assembled engine (APE) concept using the metal L-PBF process, paving the way for the future development of fully integrated, AM-driven propulsion solutions.

Methodology

The proposed engine design implicitly considers both the constraints and advantages of DMLS to achieve a fully integrated and pre-assembled architecture, following the ASTM F3530-22 guidelines for powder bed fusion [26].

Constraints and Advantages of Powder Bed Fusion. Direct metal laser sintering introduces challenges in achieving low porosity, high-strength, and dimensionally accurate parts. Careful optimization of parameters such as laser power, scanning speed, and hatching patterns is essential, particularly for complex structures and small features. Inadequate selection of the process window can lead to defects such as the balling effect, increasing surface roughness and porosity, and in severe cases, even damaging the recoater and resulting in process failure [27]. Excessive energy input can create deep penetration melt pools, known as keyholes [28], or induce strong melt pool flows driven by the Marangoni effect, leading to gas entrapment and resulting in porous, rough components [29].

The rapid heating and cooling during scanning induce thermal expansion and compression cycles, generating residual stresses that lead to dimensional deformation, especially in thin-wall structures [30]. Potentially causing microcracks or delamination [31], these stresses compromise the component's structural integrity and printability. To help reduce thermal distortion and improve surface quality, thermal management strategies can be employed, a common approach is optimized hatching patterns, typically with short scan vectors and a 67-deg rotation between consecutive layers [32].

Overhanging structures with low cantilever angles, close to horizontal, lack sufficient support from the underlying powder bed or previous layers. During the melting process, gravitational and residual stress forces can lead to increased downskin surface roughness due to dross formation [33], as well as part deformation. The out-of-plane deformation can be so extreme as to destabilize the powder bed causing uneven spreading of powder layers in subsequent steps. This instability can further compromise the part's dimensional accuracy. Moreover, limited thermal connection to the bulk material below, can cause inefficient heat dissipation, leading to localized overheating, and further deformation.

A key advantage of AM is its ability to create highly complex geometries [34], including nested self-supporting structures where multiple components can be built within one another in their operational configurations. To enable this, each component is designed not only to be self-supporting in itself but also to facilitate the build process of connected geometries above it. This integrated approach ensures manufacturability while respecting self-supported L-PBF constraints, such as limiting cantilever angles to a maximum of 55 deg relative to the vertical plane. Although the engine is manufactured essentially as two parts, a single rotating assembly and a stationary casing, each component fulfills multiple functions.

System Design for Additive Manufacturing of Pre-Assembled Gas Turbine Layout. The adoption of additive manufacturing, coupled with the elimination of traditional assembly processes, imposes unique design requirements on the gas turbine layout. Furthermore, the L-PBF method necessitates the use of a single material throughout the engine. Given that the turbine endures the most severe stresses and temperatures, the entire engine is fabricated using nickel alloys, specifically Inconel 718. The design is streamlined into two primary components: rotating and stationary parts. Both components, nested inside one another and formed simultaneously, are engineered as self-supporting structures to address the infeasibility of support removal from internal surfaces.

The inherent limitations of additive manufacturing affect various system components to different degrees. Therefore, before initiating component-level optimization, it is vital to assess constraints that significantly impair component performance and identify the ones that permit acceptable compromises. For aerodynamic components, such as compressor and turbine blades, overhang angles are particularly critical. An experimental prestudy established a critical overhang angle of 55 deg, with angles below this threshold resulting in unacceptable geometric distortions. This overhang angle limitation forms the basis of the features' design across the system, including internal cavity bores and arches, thereby ensuring printability and structural integrity.

Additional challenges arose with thin-walled elements and lattice structures, as they are highly susceptible to residual stresses, which can lead to deformation. These deformations may result in protrusions beyond the intended powder layer height, increasing the risk of recoater collisions and, consequently, print failures. To improve process reliability, a flexible silicone recoater was employed. Upon contact with deformed features, it does not cause damage but instead conforms to surface irregularities due to its flexibility. This approach helps prevent process interruptions and ensures consistent powder layer deposition. Once these component-level concerns were addressed, focus shifted to system-level integration. An iterative optimization strategy was implemented to enable continuous, defect-free printing while accounting for energy distribution (thermal gradients), structural stability, and depowdering requirements. The holistic design methodology for complex systems with multifunctional parts is schematically presented in Fig. 1.

Figure 2 illustrates the engine architecture. Both the rotating and stationary components begin with a layer of external sacrificial structures separating the parts from the build plate, for which the height is dictated by the bandsaw width used in the detachment

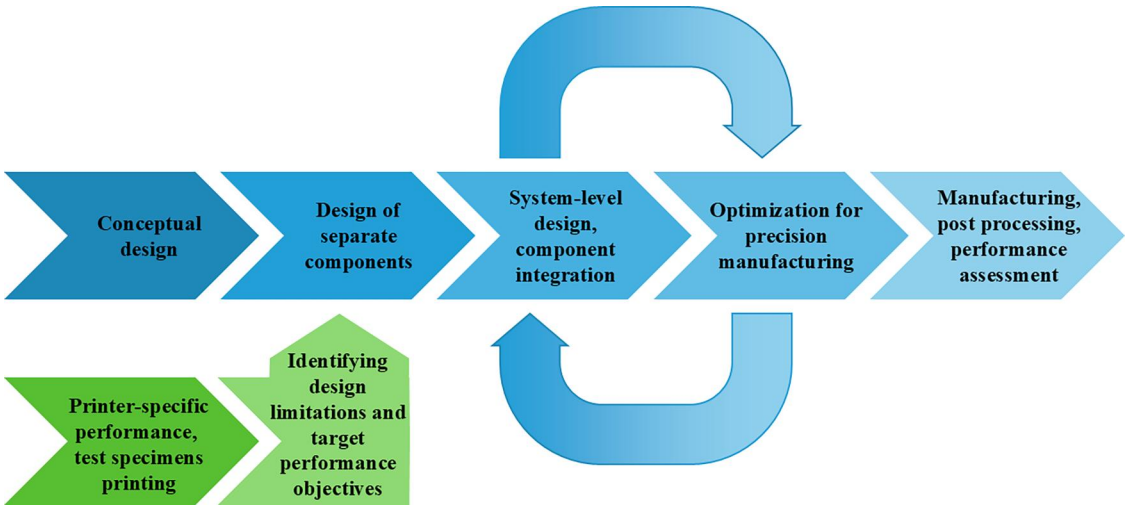

Fig. 1 Implemented design-for-additive-manufacturing approach

process. The engine's rotating element is designed to be balanced postmanufacturing through the removal of mass from externally exposed surfaces.

In the rotating inner part, the first component formed according to the build direction is the balancing weight, which also serves as the engine nozzle. In the print sequence, the mixed flow turbine blades are gradually developed from this surface according to the cantilever angle constraints. In the following, a hollow shaft is constructed, which serves as a conical journal bearing supported by hydrostatic/dynamic forces of the surrounding liquid, considering that rolling elements cannot be additively manufactured due to submicron-level tolerances required. The final component of the rotating part is the radial compressor impeller, which concludes with a growing radius hub around the inlet that serves as a balancing weight and intake. The rotating part is hollowed-out when possible, in order to reduce weight, while retaining self-supporting design principle and considering stress limitations.

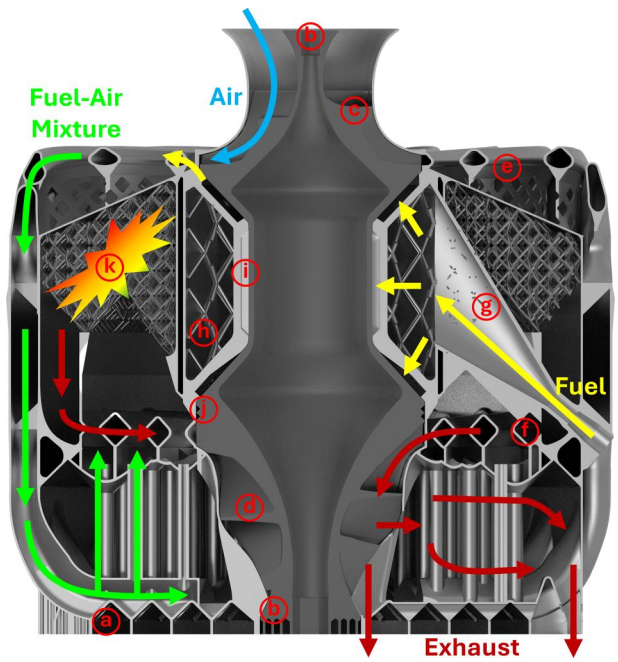

Fig. 2 Pre-assembled additively manufactured micro gas turbine layout: (*a*) external sacrificial structure, (*b*) balancing masses, (*c*) radial compressor impeller, (*d*) mixed flow turbine wheel, (*e*) fish tailpipe diffuser, (*f*) diamond-shaped turbine guide vanes, (*g*) funnel-shaped fuel pipe, (*h*) high pressure fuel manifold, (*i*) liquid hybrid bearing, (*j*) labyrinth sealing, and (*k*) porous media combustor

The stationary housing is built simultaneously around the formation of the inner rotating structure, layer by layer, and according to the build direction and the height of the fusion process in sequence. The outer part begins with the heat exchanger, which is included solely as a technological showcase for a potential future recuperator. The design, optimization, and integration of a functional recuperator represent a significant and complex challenge, and are therefore reserved for future, dedicated investigations. Although it is not considered in the current thermodynamic analysis, the heat exchanger at this stage primarily serves to refine the manufacturing process. The print sequence then progresses to the pipe-shaped inlet turbine guide vanes and the axial porous inert media (PIM) combustor, which serves as both structural support and a heat sink during the manufacturing process for the upper components. Concurrently, the high-pressure fuel manifold, which also functions as a hydrostatic bearing housing, is fabricated with an integrated lattice structure. This lattice acts as a heat sink and provides structural reinforcement, mitigating wall cracking and enhancing the rigidity of the component (minimizing deformations). To achieve a compact, lightweight design with a self-supporting structure, the sequence concludes with the incorporation of a fishtail pipe diffuser.

The resultant thermodynamic cycle is conventional for any gas turbine. The gas path is initiated with the air being sucked in through the intake and gets pressurized in the compressor impeller and the following diffusor. In the meantime, the fuel is introduced through a funnel-shaped pipe into the high-pressure manifold, where it is evenly distributed among the bearing pockets via drop-shaped orifices. Employing fuel as the lubricant (potentially mixed with small quantities of oil, as it is common in the microgas turbine industry [35]) simplifies the architecture and also removes the heat generated by the combustor and the bearing, while preheating of the fuel recycles thermal energy. To prevent fuel leakage toward the turbine and nozzle, labyrinth seals are employed on the turbine side of the conical bearing. Therefore, the fuel is exhausted to the compressor side, where it atomizes and mixes with the incoming air to form an aerosol. This premixed fuel–air mixture is then routed through a hypothetical recuperator before entering the combustor. In the currently developing configuration, which follows the investigated thermodynamic cycle without a recuperator, the fuel–air mixture flows directly into the combustor after passing through the compressor's fish tailpipe diffuser. Combustion occurs in the porous media, which offers a compact design and burns a lean mixture at reduced temperatures [36]. The resulting hot gases then undergo

acceleration in the nozzle guide vanes and expansion through the turbine wheel. The expulsion of the gases is partly through the recuperator bleed and predominantly through the nozzle Fig. 2.

Results

The dimensions of the engine are constrained by the build volume of the DMLS machine, which dictates the upper limit of the manufacturable scale. For the current exercise, the EOS M400 machine, with a build volume of $400 \times 400 \times 400mm$, is considered. The design of the turbomachinery components is also significantly influenced by L-PBF limitations, such as overhang angles, necessitating a compromise between aerodynamic performance and manufacturability with good surface finish and minimal postprocessing operations. This design approach begins with a preliminary phase where manufacturing constraints on blade angles are directly integrated, followed by a detailed design and optimization phase utilizing a gradient-based optimization technique with a Reynolds-Averaged Navier–Stokes solver and structural mechanics analysis tool to further refine the design.

Thermodynamic Analysis. To establish the initial conditions for aero component design and engine performance assessment, a 0D parametric thermodynamic analysis was conducted, focusing on the compressor pressure ratio and flowrate parameters, while maximizing the engine thrust rating serves as the objective function.

Temperature rise within the compressor and pressure drop across the turbine were evaluated using established isentropic relationships [37], with assumed isentropic efficiencies of 0.7 for both components reflecting the lower bound of the expected values. The turbine outlet temperature was calculated based on the power balance between the compressor, the bearings, and the turbine. The material limitations restricted the maximum thermodynamic cycle temperature to $1100K$ [38]. Compressor power was determined as the product of the enthalpy differential and the mass flowrate, while bearing power was modeled as proportional to the surface area (A_f) and tangential velocity (U_t) [39], which is governed by the rotational speed of the aero components, as derived from Eq. (4)

$$PB = \frac{\mu A_f U_t^2}{c} \tag{1}$$

A nominal clearance (c) of 100 μm, representing the upper limit of typical journal bearing clearances, was adopted. To compute the missing bearing area and tangential velocity in the bearing power equation, the initial dimensions of the engine's rotor were estimated.

The engine was conceptually divided into three equal-length axial sectors: the intake and compressor, the region containing the combustion chamber and bearings, and the turbine with the nozzle. The height of the bearing and combustor was assumed to be 130mm each. To allow sufficient space for axial turning of the pipe diffusers, the maximum permissible compressor diameter was set at 160mm. As an initial approximation, the mean bearing diameter was assumed to be half the compressor diameter.

The pressure drop across the proposed PIM combustor was calculated using the Ergun-type Eq. (2) [40], assuming a typical flow velocity of 90 m/s at the diffuser outlet [41]

$$\frac{\Delta P}{\Delta L} = 110\frac{\mu}{\psi D_h^2}u + 1.45\frac{\rho}{\psi^2 D_h}u^2 \tag{2}$$

where ψ represents the dimensionless porosity of the PIM, D_h denotes the hydraulic pore diameter in meters, and u signifies the upstream flow velocity in m/s. The chosen porosity value is 0.8, a parameter corresponding to a temperature of 1100 K, as documented in Ref. [42]. Assuming a perfectly expanded nozzle, the thrust calculation is performed according to Ref. [37]. Gas properties across engine stations, influenced by changes in pressure, temperature, and composition, were computed using the COOLPROP database. [43]. The outcomes of this parametric study are presented in Fig. 3.

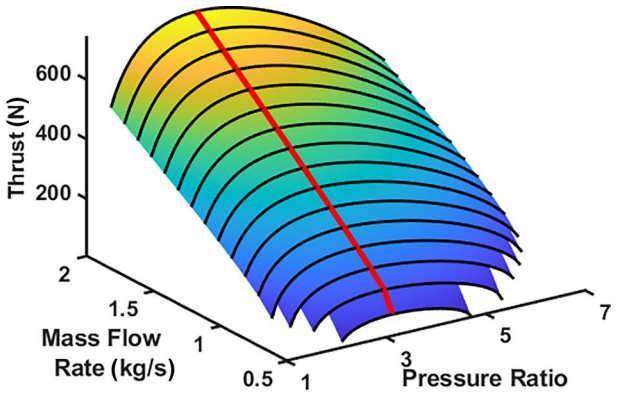

Fig. 3 Thermodynamic analysis of simple cycle microgas turbine under assumed nonisentropic processes

It is observed that peak thrust levels remain consistent across the range of flow rates at a pressure ratio of 3.2, a value significantly lower (due to low component efficiencies) than that of the ideal cycle's optimal point at ~10. Therefore, the optimization of aero-components should prioritize improving component efficiencies and maximizing the compressor flowrate to benefit power density. The parameters used to initialize the optimization routines are summarized in Table 1.

Compressor. For the compressor, the specific diameter is derived using the equation

$$D_S = \frac{D(gH)^{0.25}}{\sqrt{Q}} \tag{3}$$

where H represents the pressure head in meters and Q represents the volumetric flowrate. Within the context of a flowrate range spanning 0.5 to 2 kg/s, the specific diameter range falls between 3.3 and 6.7. Consequently, in accordance with the Cordier diagram [41], the specific speed should approximately fall within the range of 0.5–1.0, defined as

$$N_s = \frac{N\sqrt{Q}}{(gH)^{0.75}} \tag{4}$$

where N represents the rotational speed in rad/s. A specific speed of 0.5 is selected, primarily in an attempt to minimize blade stresses, which resulted in a rotational speed of 58,000 RPM. These calculations finalize a set of parameters required to begin the optimization routine.

First, a preliminary design phase is conducted, which establishes the main dimensions of the compressor, where the losses are based on correlations and include contributions from incidence, tip leakage, and diffusion (estimated based on a jet-wake model) [44].

Table 1 Performance comparison of initial and optimized engine design

Cycle	Pressure ratio	Corrected mass flow rate (kg/s)	η_{comp}	η_{turb}	η_{th}	Thrust (N)
Initial	3.20	1.40	0.70	0.70	0.063	500
Optimized	3.75	1.90	0.81	0.90	0.18	1050

The inducer of an impeller optimized for minimal inlet Mach number leads to blade angles in excess of 60 deg, which is an overhang beyond that of additive manufacturing constraints. As a result of AM constraints, the inducer tip radius is smaller than optimal, leading to a larger inlet Mach number, based on the smaller peripheral speed and the larger axial velocity for the same mass flow. This eventually leads to a stronger diffusion in the inducer with higher losses. The results obtained reveal a predicted efficiency of 75% at nominal rotational speed—slightly above the 70% assumed in the cycle analysis.

The preliminary geometry is subsequently optimized using computational fluid dynamics (CFD) and computational structural mechanics (CSM) in an automated design system, aiming to further improve the aerodynamic efficiency while lowering the mechanical stresses. The optimization is performed using a gradient-based algorithm, and the principle of the method is extensively described in Ref. [45], and briefly summarized in Fig. 4.

The geometry of the compressor is parametrized using 112 design variables which control meridional contours of the compressor, the blade angle distributions at hub and shroud, the thickness distributions, the position of the splitter blade leading edges at hub and shroud, and the hub fillet radius. Starting from the initial values of the design variables, the geometry of the compressor is generated using computer aided design and optimization (CADO) [46]. Then, the aerodynamic and structural performance is evaluated using, respectively, CFD and CSM solvers. The fluid domain is discretized using a multiblock structured mesh with approximately 1.5×10^6 cells. The aerodynamic performance of the compressor is obtained by solving the Reynolds-Averaged Navier–Stokes equations with the Spalart–Allmaras turbulence model. The CFD solver used in the context of this work is extensively discussed in Ref. [47]. In the solid domain of the compressor, an unstructured mesh is generated using tetrahedral elements, and the structural analysis is performed using a finite element method, detailed in Refs. [48] and [49]. The gradients of the aerodynamic and structural cost functions with respect to the design variables are evaluated using the adjoint capabilities of the CFD and CSM solvers. These gradients provide useful information on how to modify the shape to improve the performance. A sequential quadratic programing method recuperates gradients from previous cycles of the search, enhancing significantly the pursuit of the optimal shape.

The objective is to maximize the mass-flow in order to increase the thrust-to-weight ratio. Total-to-total efficiency of the compressor is selected as a constraint, and the lower limit is specified as the value obtained for the baseline compressor, evaluated to be 77.9% by CFD. Additionally, a structural constraint should prevent the optimizer to look for aerodynamic gains that are mechanically unfeasible. In the as-manufactured state, the yield strength values of additively manufactured Inconel 718 are 650 MPa, and 800 MPa in the vertical and horizontal directions, respectively [50]. After applying heat treatment according to AMS 2774 and AMS 5662

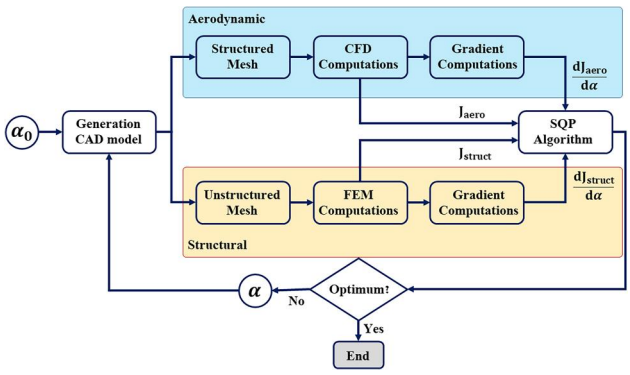

Fig. 4 Flow chart of aerodynamic-structural turbomachinery optimization algorithm

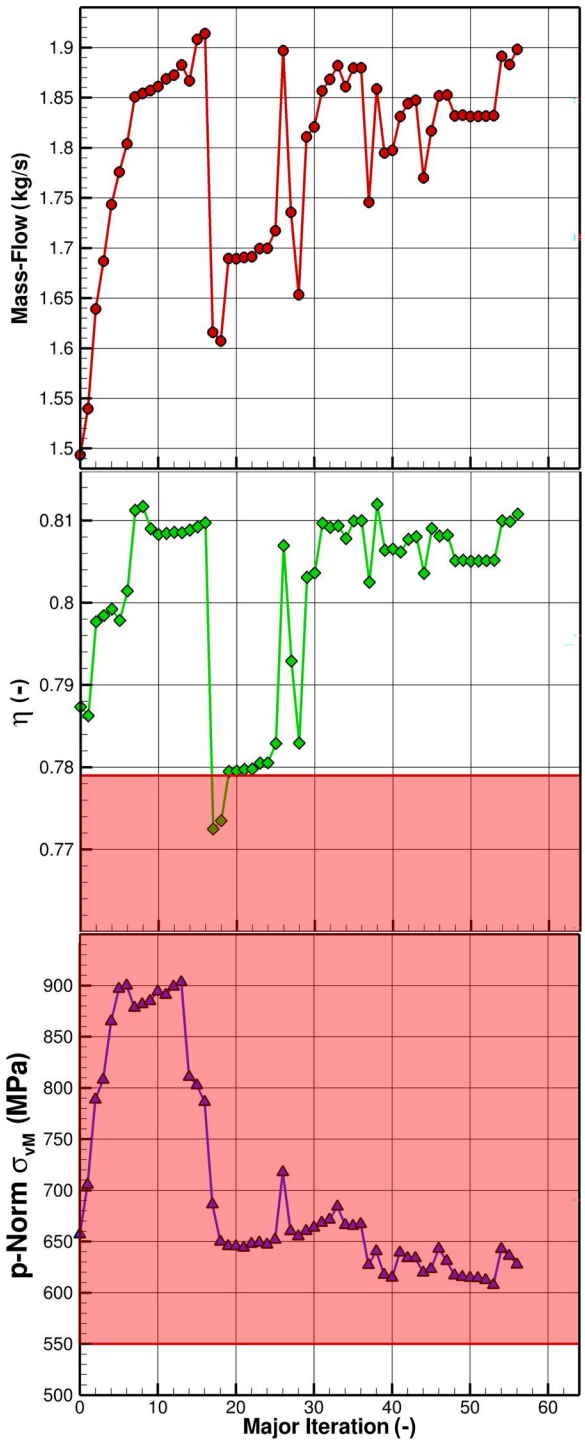

Fig. 5 Optimization convergence history of parametrized compressor geometry. Top: mass flow objective, middle: efficiency constraint and bottom: stress constraint.

standards, the yield strength values increase to 1145 MPa, and 1240 MPa in the vertical and horizontal directions [50]. To effectively capture structural performance while avoiding oversensitivity to localized stress peaks, the volume-weighted p-Norm stress approximation is used as a surrogate for the maximum von Mises stress. This method emphasizes broader regions of high stress rather than isolated peaks and provides a more robust assessment of structural risk. Because it tends to underestimate the true local maximum stress, a lower target stress value is chosen to ensure the design remains within the required safety margin. In this study, the maximum p-Norm stress is constrained to be below ~550 MPa,

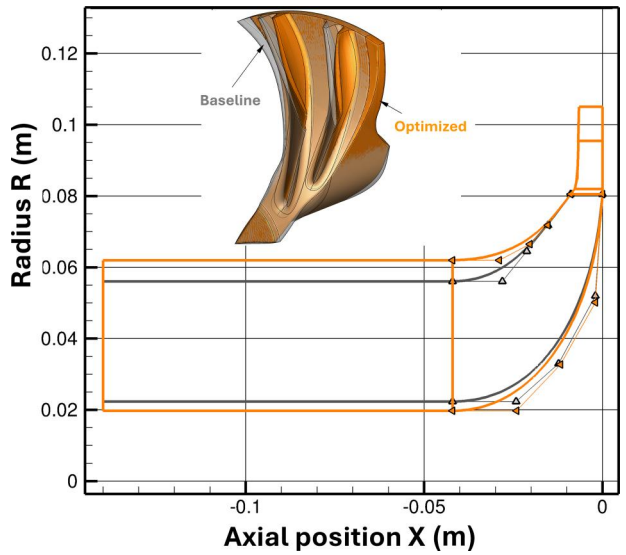

Fig. 6 Meridional path and 3D layout comparison of baseline and optimized radial compressor layout: initial (transparent) and optimized (solid) (Color version online)

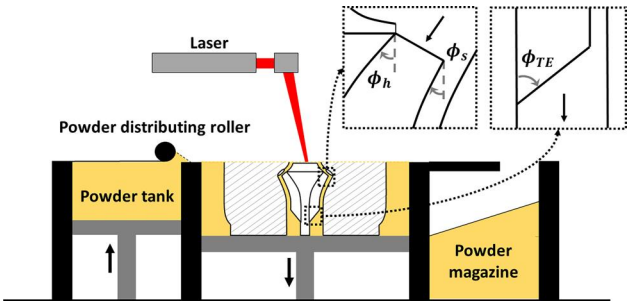

Fig. 7 Geometric constraints of self-supported turbine design for powder bed fusion

which provides a safety factor between ~1.2 and 2 depending on the heat treatment.

Figure 5 illustrates the convergence histories of gradient-based optimization. The darker regions represent the areas where the efficiency and stress constraints are not satisfied. After 56 major iterations, the mass flow is increased to 1.90 kg/s while the total-to-total efficiency also rises to 81%. The constraint on the von Mises stress is more difficult to satisfy, as high mass flows lead to large blades, which in turn lead to large centrifugal stresses. The imposed target is thus probably not reachable, and the optimizer has been searching for a design that is closest to satisfying the requirement while keeping a high mass flow through the impeller. While the optimization did not meet the targeted p-Norm, it successfully maintained the maximum corresponding von Mises stress at 790 MPa, a postheat treatment safety factor of 1.45, which is considered satisfactory within the scope of this study. Summarizing the findings, Fig. 6 compares the 3D geometries and the meridional contours of the baseline and optimized compressors. The results indicate that the baseline geometry has been significantly modified during the optimization process, especially the meridional channel, which has been enlarged in order to increase the mass-flow in the compressor.

Turbine. The turbine inlet condition is adapted according to the upstream components. It has been assumed that 5% of the total pressure built in the compressor is lost inside the combustion chamber (leading to $P_0 = 357$ kPa). The inlet total temperature is set according to the combustion chamber exit limit conditions, $T_0 = 1100$ K. Regarding the turbine outlet, atmospheric pressure can be assumed at the hub, while the radial equilibrium is considered for all other radii. Moreover, the turbine transfers power to the compressor through the shaft, with part of this energy dissipated in the bearings, estimated at 30 kW according to Eq. (1). Moreover, the turbine mass flowrate should match that of the compressor, with the fuel mass flowrate assumed negligible. The matching conditions considered are 1.90 kg/s ±1% and 341 kW ±3% for turbine mass flowrate and power, respectively.

Comprising 10 blades and a backplate, with a tip clearance of 0.6 mm, the design of the radial turbine is highly influenced by additive manufacturing constraints associated with self-supporting structures, necessitating a transition to a mixed-flow configuration. The layer-by-layer manufacturing process, particularly from the trailing-edge to the leading-edge, demands careful attention to the meridional channel and its parametrization. Key structural angles, including those for the hub and shroud blade inlet angles (ϕ_h and ϕ_s) and the trailing-edge cutback (ϕ_{TE}), are constrained to remain below 55 deg relative to the vertical plane to ensure manufacturability. As portrayed in Fig. 7, The position of the hub and shroud points near the blade inlet is controlled using angular and distance parameters (ϕ_h, ϕ_s, and d_h,d_s) instead of traditional X-Y coordinates. Incorporating slight modifications to the meridional contour parametrization, the turbine is characterized through the solid blade angle β distribution at the hub and the shroud, the blade bowing $\Delta\theta$ at midspan and the blade thickness distribution at hub, shroud and midspan sections. Additional parameters are the inlet rake angle and hub fillet radius, for a total of 63 free parameters. A single channel domain is considered with periodic boundary conditions and the fluid domain is discretized using a multiblock structured mesh comprising $\sim 1.3 \times 10^6$ cells, while the solid domain is discretized with an unstructured mesh consisting of $\sim 0.5 \times 10^6$ tetrahedral elements.

In the following, the turbine is optimized using the same framework as the compressor and imposing maximum p-norm stress of ~580 MPa (yielding a postheat-treatment safety factor of 1.98). Presented in Fig. 8, the optimization history shows convergence after 31 iterations, with the isentropic total-to-total efficiency increasing from 87.3% to 89.6%. Stresses are significantly reduced to satisfy the imposed upper p-Norm bounds, resulting in a maximum von Mises stress of 696 MPa, corresponding to a safety factor of 1.65, while both power and mass flow rates remain at their respective constraint limits. A comparison of the initial and optimized geometries, shown in Fig. 9, highlights the design modifications. The blade bowing and inlet rake angles are reduced, resulting in a blade configuration closer to a radial structure and lowering the induced stresses at midspan. Additionally, the near shroud blade inlet section radius is increased, effectively reducing the average velocity in the channel. Enhancements to the hub fillet radius contributed to reduced stress near the hub, and improvements to the blade camber minimized the effects of secondary flows, thereby reducing the entropy generated.

Combustor. After finalizing the aerodynamic components, the axial porous inert media combustor dimensions need to be estimated, considering the EOS M400 printer's build volume as the upper bound. As an initial step in the design process, the flammability limits of the premixed kerosene–air stream are investigated. The analysis is performed using the commercial software ANSYS CHEMKIN-PRO, employing a perfectly stirred reactor model. The reactor volume is adjusted to reflect a porosity of 0.8. The chemical kinetic mechanism is sourced from the CRECK Modeling Group [51], which offers a comprehensive framework for the pyrolysis, partial oxidation, and combustion of hydrocarbon fuels. This mechanism includes up to 16 carbon atoms and covers alcohols, esters, and representative surrogate components for real fuels. The kinetic scheme comprises 492 species and 17,790 reactions. Kerosene is represented by the San Diego surrogate fuel,

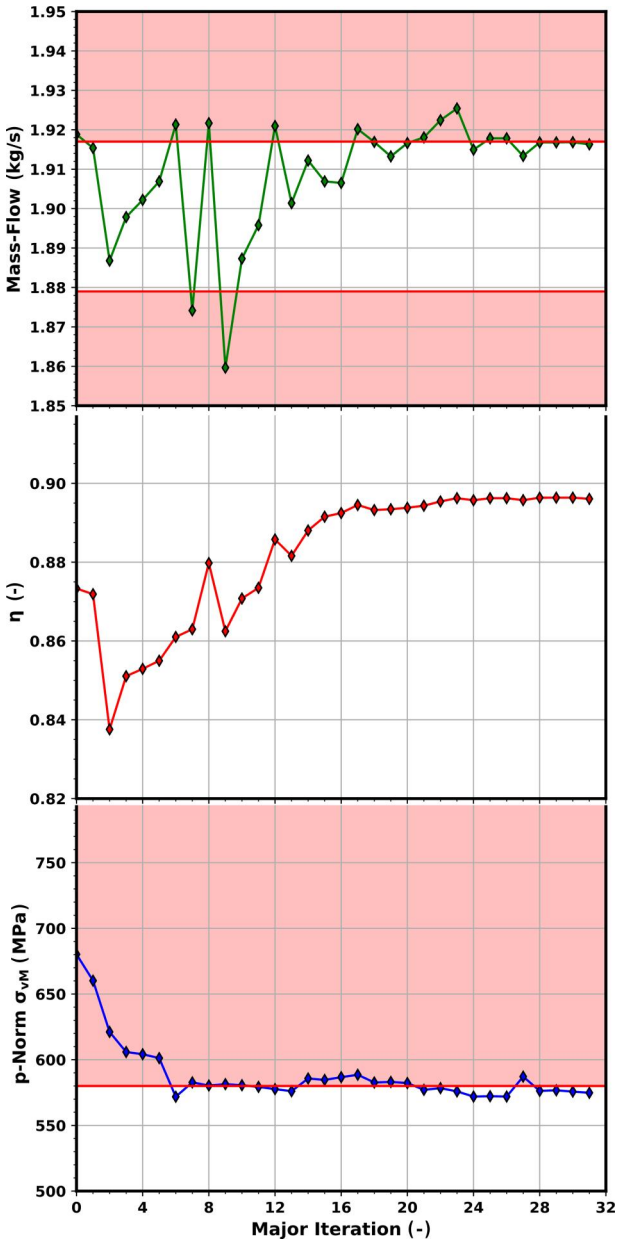

Fig. 8 Optimization convergence history of parametrized turbine geometry optimization top: efficiency constraint, bottom: stress constraint

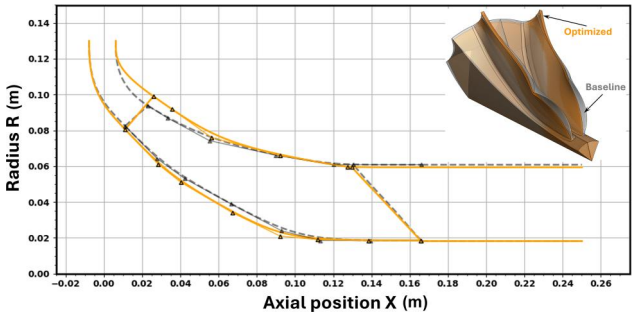

Fig. 9 Meridional path and 3D layout comparison of baseline and optimized mixed-flow turbine layout: initial (grey) and optimized (orange) (Color version online)

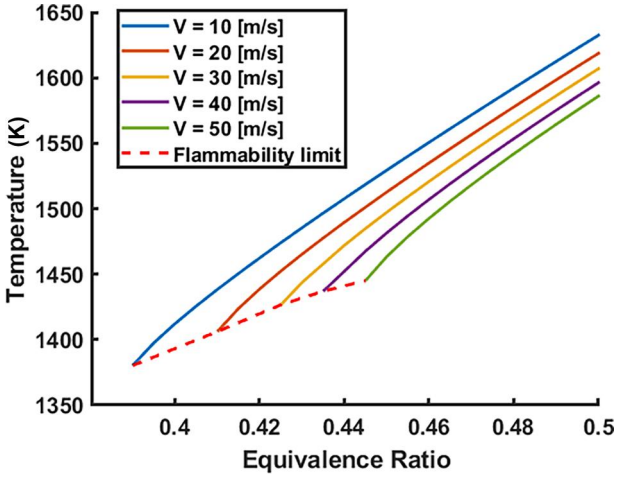

Fig. 10 Porous inert media flammability limits for different upstream flow velocities according to CHEMKIN simulations without heat transfer and radiation effects

consisting of *n*-decane $C_{10}H_{22}$ (60%), Methylcyclohexane C_7H_{14} (20%), and toluene C_7H_8 (20%) [52].

The results across various mixture advective velocities from 10-50 m/sec, shown in Fig. 10, reveal flammability limits ranging from equivalence ratios of 0.39–0.5, yielding adiabatic flame temperatures above the target of 1100 K under the engine's design conditions. While these results provide valuable insights, they do not account for heat transfer and radiation effects in the PIM combustor's lattice structure. Nevertheless, they guided the determination of the combustor's outer diameter and the initial equivalence ratio values for subsequent CFD analyses.

Accordingly, the axial PIM combustion chamber is formed of uniform isotruss lattices with 80% porosity and 10 PPI, with dimensions of 380 mm and 160 mm for the outer and inner diameters, respectively, at a length of 130 mm. This configuration enabled effective deceleration of the upstream flow to approximately 10 m/s, enhancing flammability limits and minimizing pressure loss. The ensuing ANSYS FLUENT simulations are conducted on a partial 10-deg sector of the combustor with periodic boundary conditions, due to computational constraints. Comprising 1.1 and 1.8×10^6 polyhedral cells in the solid and fluid zones of the domain, respectively, a steady-state coupled conjugate solver is implemented with a realizable k–ε turbulence model. Additionally, a discrete ordinates radiation model is employed assigning an absorption coefficient of 1×10^7 m^{-1}. The inlet conditions are configured to match the compressor outlet parameters, with upstream combustor velocities ranging from 10 to 50 m/s. For combustion modeling, an eddy dissipation model is applied using the following chemical reaction:

$$C_{12}H_{23} + 17.75O_2 \rightarrow 12CO_2 + 11.5H_2O \quad (5)$$

Then, equivalence ratios corresponding to the flammability limits, determined in the CHEMKIN analysis, are assigned for each velocity stream.

A series of simulations for various combustor inlet velocities identified the case with an upstream velocity of 20 m/s and an equivalence ratio of 0.41 as the closest match to the thermodynamic cycle parameters used in the engine component design. Figure 11 depicts the flame front in the second combustor cell, where the highest temperatures are observed in both the gas phase and the solid structure. As combustion progresses, by-product gases cool, leading to an average outlet temperature of 1038 K. Heat extracted from the flow is transferred through the solid structure, preheating the upstream air–fuel mixture, as observed in the inlet cell. The solid structure's temperature remains below 1186 K, ensuring safe operation well under the melting point of Inconel 718. The pressure

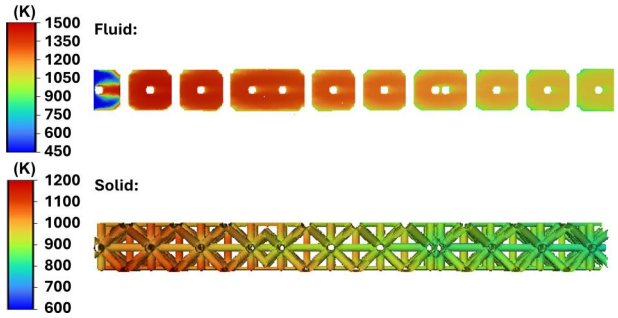

Fig. 11 Combustor temperature distribution

drop across the combustor is calculated to be 3.1%, remaining within acceptable limits below the targeted 5%. These findings establish the final combustor diameter as 253 mm, which aligns with the engine's flowrate and inlet velocity. This parameter finalizes the combustor design and defines the engine's outer dimensions.

Hybrid Conical Bearing. Leveraging both hydrostatic and hydrodynamic effects, a high-speed hybrid, fuel-driven, double-cone fluidic bearing is proposed to generate axial and radial forces toward stabilizing the rotor inside the stationary housing. A preliminary analysis assumes a steady-state equilibrium position for the bearing journal with an eccentricity ratio of 0.5, a recommended value for safe maximum load [53]. The rotor is estimated to weigh approximately 7.5 kg, and based on the G2.5 balance quality standard [54] for turbomachinery, the unbalance is estimated as 214 N. Nevertheless, the journal is expected to experience inherent vibrations, characterized by small oscillations around the equilibrium point, with an amplitude of roughly 1% of the bearing clearance [55]. This reciprocating motion introduces additional radial forces. Serving as the upper bound, the bearing stability is constrained by "half-speed whirl" [39], where the journal's angular orbit velocity is half the rotor's speed. Then, considering contributions from unbalance, gravitational, and radial forces, the total radial load can be estimated as 422 N.

In the following, the necessary fluid pressure difference P_s can be calculated from:

$$\bar{W} = \frac{W}{P_s L D} \tag{6}$$

where W represents bearing load and $\bar{W}$ is a normalized empirical load factor, equal to 0.073 for the given bearing type and corresponding eccentricity of 0.5 [53]. To enhance bearing stiffness and stability, a 20% safety margin is added to this minimum pressure, resulting in a required differential pressure of 6.3 bar. Considering that the bearing operating pressure is 3.7 bar, which corresponds to the compressor exit pressure, the required fuel inlet pressure is estimated to be 10 bar.

The hybrid bearing design is a compromise between losses and the load capacity [53]. In the presence of high shaft tangential velocities and increased clearances, it is rather difficult to accurately predict performance from 0D relations. As a first iteration, the entire length of the 130 mm sector is considered to be actively load-bearing, resulting in a mean diameter of 85 mm. Each side features a conical section of L/2 = 65 mm with a typical layout consisting of four equally spaced rectangular pockets, each 30° in peripheral span, 6 mm in depth, with a land-to-pocket ratio of 0.25 and a length-to-diameter ratio of 0.5, as illustrated in Fig. 12. Due to the L-PBF limitations an unusually large clearance value of 300 μm is adapted. Based on the analysis findings, the active bearing length can be adjusted by introducing sealing surfaces on either side of the conical surface, thereby scaling the bearing's load capacity. Furthermore, the reduction in the bearing's mean radius decreases the surface

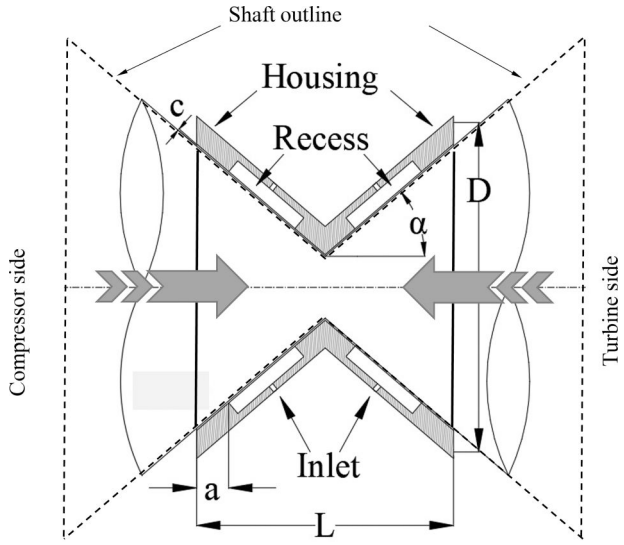

Fig. 12 Self-supported hybrid conical bearing and shaft configuration, and scaling procedure for limiting the effective bearing surface

tangential velocity and effective bearing area, allowing the bearing losses to be estimated using Eq. (1).

In order to analyze the geometry at a higher level of fidelity, an ANSYS FLUENT analysis is conducted, using a pressure-based steady-state multiphase solver with a realizable k-ε turbulence model and enhanced wall treatment. As a result of a mesh sensitivity analysis monitoring torque, flowrate, and load deviations, it is observed that the fluid domain can be discretized using a structured hexahedral mesh with 48 layers, resulting in a total of 1.53×10^6 elements. The simulation framework is verified against the benchmark hybrid bearing test case of Guo et al. [55], who conducted comparisons between the CFX-TASCFLOW [56] and VT-EXPRESS [57] tools. For this exercise, the test configuration considered is a layout with 30 mm in diameter and 20 mm in width, and a radial clearance of 0.03 mm, featuring four evenly distributed pockets, each with a peripheral span of 45 deg and an axial land of 5 mm, a depth of 1 mm, and an inlet orifice diameter of 0.6 mm. The comparison across the solvers revealed a maximum disparity of 2.1%, 0.5% and 6% in pocket inlet pressure, load capacity, and mass flowrate, respectively.

In the following, the same CFD framework is applied to the engine's conical bearing, using kerosene as the working fluid, with a liquid viscosity of 2.4 cP and a gas-phase viscosity of 0.007 cP. Figure 13 illustrates the recess vorticity, pressure, skin friction, and vapor volume fraction (cavitation). The bearing's eccentricity leads to an asymmetric pressure field, with rising pressure toward the minimal bearing gap, peaking at 5.98 MPa in localized zones. On the opposite side of the journal, a pressure drop occurs. In regions where the local static pressure falls below the fluid's vapor pressure, a phase change is initiated, forming cavitation pockets.

An axial pressure gradient is observed from the sealed turbine side to the open compressor side, where the fluid is discharged into the diffuser. Due to the reduced pressure on the compressor side of the bearing, the occurrence of cavitation is more prominent in this region. Representing system losses, skin friction is distributed nonuniformly. The interaction between the stationary deep recess and the high-speed tangential velocity of the shaft generates intense circulation and vortical flow (Fig. 13(*b*)), resulting in regions of high shear and elevated skin friction. In contrast to lower-viscosity cavitation regions around the landing zones, the tangential acceleration from the recess to the land homogenizes the flow, reducing skin friction on the shaft surface Fig. 13(*a*).

Looking at the integral performance metrics for the full-length bearing, the radial and axial loads are 84 kN and 29.5 kN, respectively, at a shaft power consumption of 680 kW. By the introduction of seals, scaling the active bearing half-length and

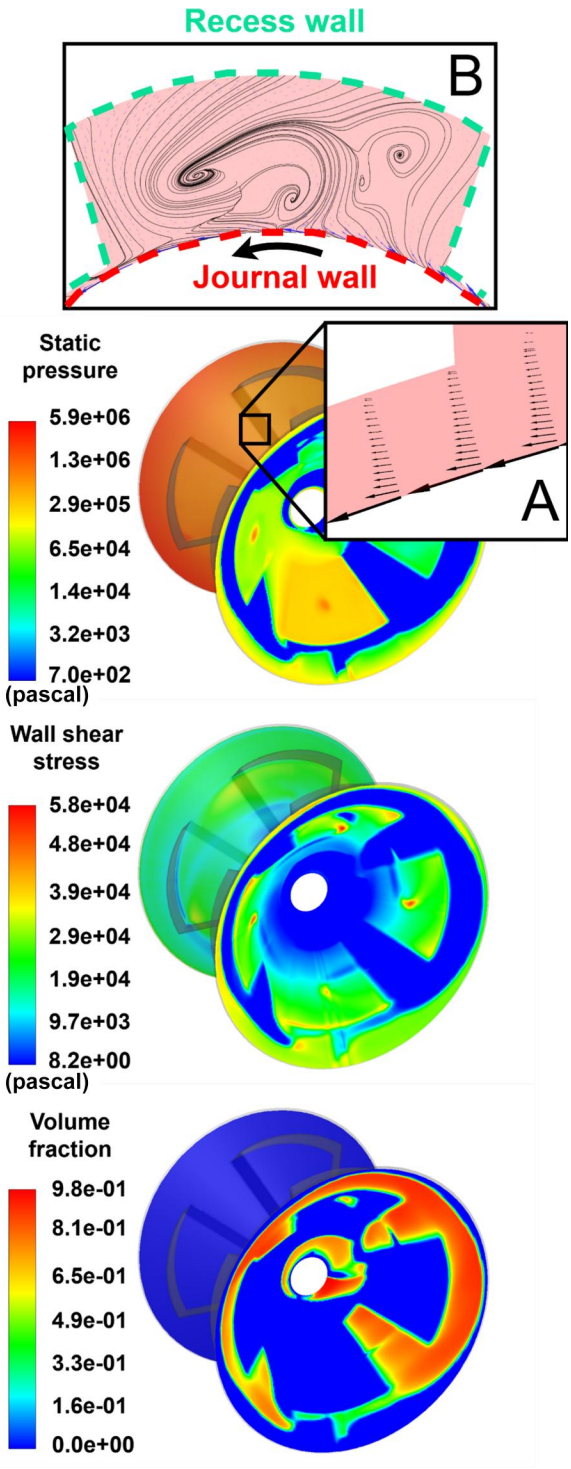

Fig. 13 CFD results of the hybrid bearing: (top) static pressure, (middle) skin friction, (bottom) vapor volume fraction: (*a*) flow transition from recess to land and (*b*) recess vortices

mean diameter to 53.5 mm and 70 mm, respectively, it is possible to reach the target bearing power of 30 kW, while still providing axial and radial load bearing capacities beyond that of the requirement, in the orders of 3.5 kN and 1.3 kN, respectively.

Manufacturing Feasibility

To evaluate the printability of the proposed pre-assembled engine concept, a manufacturing trial was conducted using the EOS M 290 L-PBF system to fabricate the proposed gas turbine layout with a 300 μm clearance between the rotor and the stationary part. The system features a Yb-fiber laser operating at a wavelength of 1080 nm, with a maximum power output of 400 W and a scanning speed of up to 7 m/s. The process utilizes spherical Inconel 718 powder (14–63 μm particle size) sourced from EOS, with its chemical composition detailed in Table 2. To prevent oxidation and other undesirable chemical reactions, printing is performed in a controlled environment with a technical-grade argon atmosphere. Working on a 316 L stainless steel build plate, a stripe-based scanning strategy is employed, utilizing 10 mm-wide stripes with zero overlap, with each successive layer rotated by 67 deg. The specific printing parameters are summarized in Table 3.

During the L-PBF process, different regions of a component experience varying numbers of heating and cooling cycles [58]. As a result, these thermal cycles induce residual stresses [59,60]. While residual stresses are not always critical, they can lead to several issues. When stresses in a specific region exceed the material's strength, failure may occur. Depending on the location, this can lead to detachment from the build platform, separation from the support material, or delamination from a previous layer. Additionally, high residual stress levels increase the material's susceptibility to crack formation during melting [61]. Residual stresses can also cause deformations in various regions of the part during printing. Thin-walled sections (less than 0.5 mm thick), overhanging geometries, and configurations with low structural rigidity are particularly vulnerable. These deformations may lead to collisions with the recoater, potentially resulting in print failure. Throughout the L-PBF process, the residual stresses are partially mitigated by the rigid fixation of the part to the build platform, either directly or through support structures. This constraint helps minimize deformation during manufacturing. However, once the part is removed from the build platform, the previously constrained residual stresses redistribute, leading to displacement relative to the intended geometry. These displacements can reach several millimeters in magnitude [62].

To predict residual stresses and their impact on the geometric accuracy of the manufactured assembly, a finite element method is employed using Simufact Additive, thermomechanically simulating both the building process and postprocessing operations [63]. Initially, a heat transfer analysis determines the thermal history, providing the temperature distribution at each nodal point, followed by a mechanical analysis, which evaluates the stresses and deformations induced by temperature fluctuations, predicting the displacement of the part relative to its nominal geometry.

Figure 14 presents the distribution map of residual von Mises stresses throughout the volume of the pre-assembled structure after manufacturing and powder removal, but before its detachment from the build plate. As shown in Fig. 14, the principal stresses range from 500 to nearly 800 MPa. An exceptionally high value is observed in a

Table 2 The chemical composition of Inconel 718 powder used for manufacturing

Element	Fe	Ni	Cr	Nb	Mo	Ti	Al
Wt.%	Balance	54.06	18.64	5.16	3.11	1.00	0.52

Table 3 Process parameters considered for the printing procedure

Laser scanning parameter		Laser scanning strategy	
Laser power (P)	285 W	Stripe width (S_W)	10 mm
Scanning speed (V)	960 mm/s	Stripe overlap (S_O)	0 mm
Powder layer thickness (t)	40 μm	Start angle (α_S)	45 deg
Hatch distance (h)	120 μm	Rotation angle (α_R)	67 deg
Focus diameter	100 μm	Contour	2
Volume energy density	62 J/mm^3		

section of the casing, where the residual stress reaches 975 MPa. This increase can be attributed to a local reduction in structural rigidity in this area due to the thinner wall structure. Moreover, generally higher residual stresses are observed in the rotor, particularly at the edges and base of the turbine blades, reaching 942 MPa and 956 MPa. Nevertheless, the overall residual stress distribution remains nearly symmetric and below the yield strength of Inconel 718 [50], suggesting sufficient rigidity. Despite being within the safe limits for bulk materials, the local stress concentrations around small features have high likelihood for crack initiation [64].

Following manufacturing, powder removal, and detachment from the build platform, the distribution of total displacements within the volume relative to its nominal CAD model is illustrated in Fig. 15. Most displacements fall within the range of –0.3 to 0.3 mm. However, significantly larger local displacements up to 1.0 mm are observed in the casing regions corresponding to high residual stresses. The displacement distribution is more asymmetric than the stress distribution, likely due to the nonuniform relaxation of residual stresses during the build-plate detachment process. Obviously, the most critical area is associated with the interface between the rotor and the surrounding housing, where a nominal 300 μm gap is desired. The simulation predicts that the bearing clearance is highly nonuniform (260–120 μm) in most locations, and in certain areas, the clearance diminishes to zero, indicating contact/crash between the rotation and stationary parts.

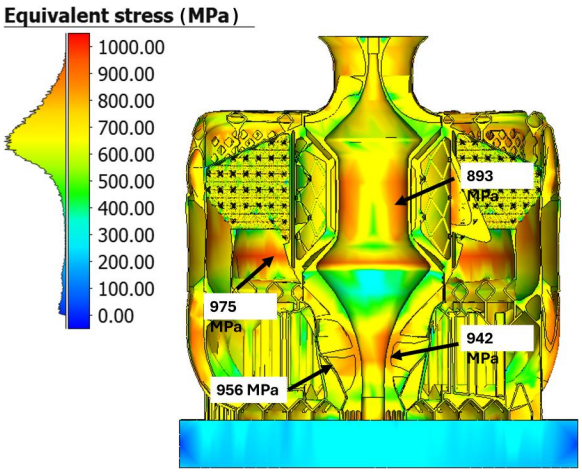

Fig. 14 Equivalent stress distribution of nominal engine architecture under thermomechanical simulation of laser powder bed fusion, predetachment from build-plate

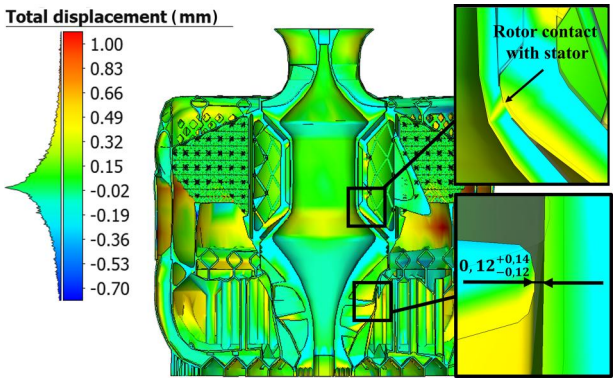

Fig. 15 Total displacement distribution of nominal engine architecture under thermomechanical simulation of laser powder bed fusion, postdetachment from build-plate distribution

To offset distortions and ensure geometric accuracy, a precompensation method is implemented. This approach introduces artificial deviations into the geometry to counteract predicted displacements. Specifically, a compensation factor of -1 is applied to the forecasted displacements obtained from the thermomechanical model. The negative sign signifies that predeformations are imposed in the opposite direction of the simulated displacements. This process of precompensation optimization is iteratively repeated with feedback from thermomechanical simulations until the desired postbuild geometric accuracy is achieved.

As a result of this procedure, the displacements after precompensation optimization are illustrated in Fig. 16, with most of the values ranging between ± 70 μm. In the outer casing, there is a slightly higher displacement peak of $+400$ μm due to low stiffness, however, this region is not critical for the engine performance and can be easily compensated by the rigid interface to the platform. Most importantly, the critical geometrical accuracy of targeted 300 μm clearance between rotating and stationary parts is uniformly preserved.

Before manufacturing the additively manufactured preassembled engine, the accuracy of the precompensation method and feasibility of fabricating nested structures are assessed in a representative double-cone topology, with a clearance of 300 μm and a cantilever angle of 45 deg. Figure 17 presents the total displacement distribution of the double-cone obtained via the precompensation method, along with the fabricated and sectioned cone. The double-cone achieved the targeted 300 μm clearance, with deviations of up to –30 μm between sliding surfaces and surface roughness below Ra 6.3 μm across all surfaces, demonstrating the reliability of process.

Finally, the same additive manufacturing process for preassembled nested architecture is applied to the APE gas turbine

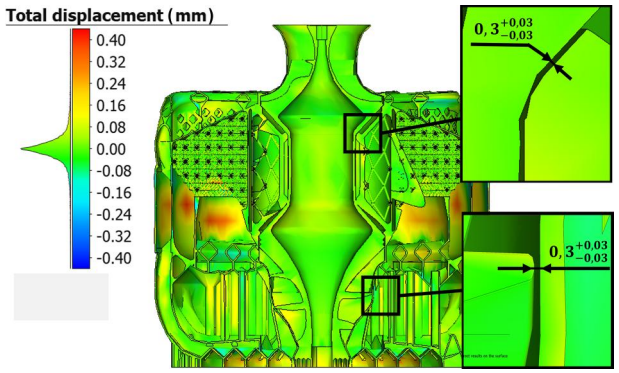

Fig. 16 Total displacement distribution of precompensation optimized engine architecture under thermomechanical simulation of laser powder bed fusion, postdetachment from build-plate distribution

Fig. 17 Precompensation and manufacturing method validation by 45 deg double cone geometry with 300 μm clearance

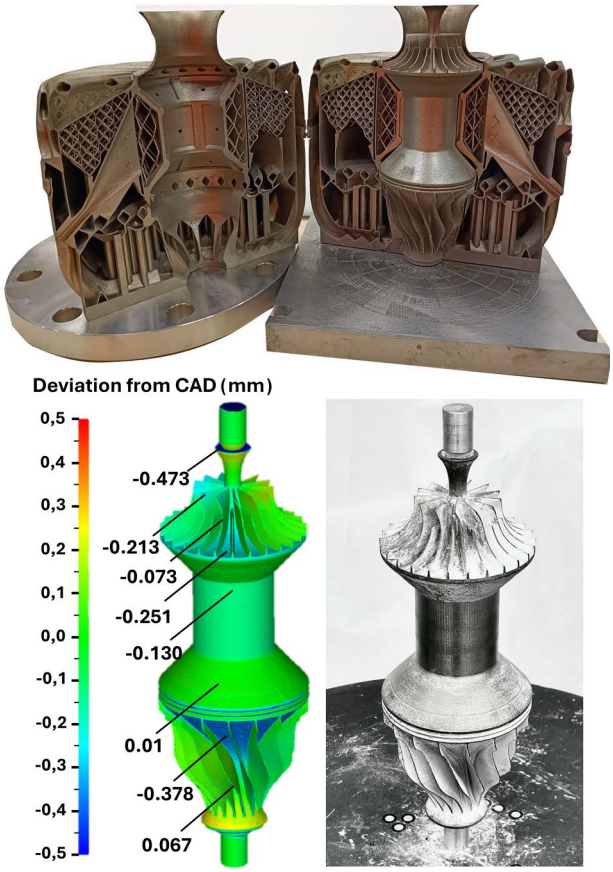

Fig. 18 Additively manufactured pre-assembled micro gas turbine engine fabrication technology demonstrator (top) and deviation of the rotor from the nominal CAD geometry (bottom)

layout. Figure 18 portrays the bisectioned engine after powder removal and detachment from the build platform. A visual inspection confirmed satisfactory component quality, with the rotor freely positioned inside the stator and maintaining a uniform clearance. The clearance values measured using feeler gauges in the critical hybrid conical bearing region ranged from 225 μm to 250 μm. The cylindrical bearing segment exhibits a lower surface roughness of Ra 3.2 μm, while all other surfaces maintain roughness levels below Ra 6.3 μm.

By scanning the rotor with a ZEISS COMET L3D scanner, a high-precision assessment of geometric deviation from the nominal CAD model is conducted. Figure 18 presents the rotor's relative deviation distribution. The conical segment of the hybrid bearing demonstrates high accuracy, exhibiting a mere deviation of 10 μm. Both the compressor and turbine blades yield satisfactory results, with blade tip deviations of –73 μm and –67 μm, respectively, aligning closely with the predicted ranges. However, higher local deviations are observed on the compressor blade surfaces and the turbine/compressor hub areas, averaging –213 μm, –251 μm, and –378 μm, respectively. The maximum deviation of –473 μm is recorded on the noncritical external balancing weight surface. Although not essential, the discrepancies between predicted and measured values can be further improved by calibrating the SIMUFACT ADDITIVE software's thermal cycle model for the specific L-PBF machine.

Summary and Conclusions

This paper describes an innovative design-for-additive-manufacturing methodology for the realization of pre-assembled microgas turbine via laser powder bed fusion. The engine layout consolidates the entire system into two nested components build simultaneously: (1) a monolithic rotor—integrating both the compressor and turbine, connected by a shaft that serves as the journal of a fluidic bearing—and (2) a stationary part incorporating turbomachinery stators, bearing housing, and an embedded porous inert media combustor. Each component is designed not only to be self-supporting in itself but also to facilitate the build process of connected geometries above it, enabling fabrication of an entire engine through a single uninterrupted print process.

The DfAM approach was systematically applied to ensure peak performance under additive manufacturing constraints such as maximum cantilever angles, minimum feature gaps, and support-free geometries. Through a comprehensive gradient-based optimization process, a radial compressor and a mixed-flow turbine are developed, enhancing aerodynamic efficiency, pressure ratio, and mass flowrate while ensuring mechanical integrity. The combustion temperature is constrained by the material properties of Inconel 718, with a maximum operational limit of 1100 K. To achieve the required temperature in a premixed combustor, a lattice is designed with 0.8 porosity and 10 PPI, facilitating the combustion of lean fuel–air mixtures. Another critical component influencing engine performance is the hybrid fuel-driven fluidic bearing. A simplified design method for the hybrid conical bearings is discussed, scaling bearing areas to meet power demand and load-bearing requirements. These component-level improvements significantly enhanced the engine performance, ultimately increasing thrust from the initial estimations of 500 N to 1050 N, as indicated in Table 1.

The manufacturability of the engine is validated through experimental printing on an EOS M290 machine. To realize high geometric accuracy, precompensation optimization techniques are applied to counteract distortions caused by residual stresses during the laser sintering process. For all critical parts, the geometric deviation between the printed engine and its nominal CAD design is measured to be within ± 70 μm, with surface roughness in the range of Ra 3−6 μm.

The successful feasibility demonstration of an additively manufactured, pre-assembled microgas turbine represents a significant step toward the next generation of propulsion systems. By implicitly incorporating capabilities and constraints of additive manufacturing into system design, this research highlights a scalable and cost-effective approach to future turbomachinery development.

Funding Data

- NATO Science for Peace and Security Program (Grant No. G5939-Additively Printed Engine (APE); Funder ID: 10.13039/100004415).

Nomenclature

a = bearing land length (m)
A_f = effective bearing surface area (m^2)
c = nominal bearing clearance (m)
D = diameter (m)
d_h = turbine hub diameter (m)
d_s = turbine shroud diameter (m)
D_h = hydraulic pore diameter (m)
D_s = specific diameter
g = gravitational acceleration (m/s^2)
H = pressure head (m)
L = length (m)
N = speed of rotation (rad/s)
N_s = specific speed
P = pressure (Pa)
P_s = bearing inlet supplied pressure (Pa)
P_0 = total pressure (Pa)
Q = volumetric flow rate (m^3/s)
T_0 = total temperature (K)
u = flow velocity (m/s)
U_t = surface tangential velocity (m/s)
W = bearing load capacity (N)
$\bar{W}$ = normalized bearing load capacity
α = conical bearing angle (deg)

β = solid blade angle (deg)
η = efficiency
η_{th} = engine thermal efficiency
μ = viscosity (Pa·s)
ρ = density (kg/m^3)
ϕ_h = turbine inlet hub angle (deg)
ϕ_S = turbine inlet shroud angle (deg)
ϕ_{TE} = turbine trailing edge angle (deg)
ψ = porosity

Abbreviations

AM = additive manufacturing
APE = additively manufactured pre-assembled engine
CAD = computer-aided design
CADO = computer-aided design and optimization
CFD = computational fluid dynamics
CSM = computational structural mechanics
DMLS = direct metal laser sintering
DfAM = design for additive manufacturing
L-PBF = laser powder bed fusion
LEAP = leading edge aviation propulsion
PIM = porous inert media
PPI = pores per inch

References

[1] 360iResearch, 2024, "Aircraft Micro Turbine Engines Market by Engine Type," 360iResearch, Vimannagar, Maharashtra, India, Report No. MRR-5A2C6AA66BB0.
[2] Market Data Forecast, 2024, "Global Aircraft Micro Turbine Engines Market Size, Share, Trends & Growth Forecast Report," Market Data Forecast, Telangana, India, Report No. 10563, accessed Feb. 21, 2025, https://www.marketdataforecast.com/market-reports/global-micro-turbine-engines-market
[3] Fortune Business Insights, 2024, "Aircraft Micro Turbine Market Size, Share & Covid-19 Impact Analysis, By Micro Engine Type," Fortune Business Insights, Maharashtra, India, Report No. FBI105863.
[4] Khorasani, M., Ghasemi, A., Rolfe, B., and Gibson, I., 2022, "Additive Manufacturing a Powerful Tool for the Aerospace Industry," Rapid Prototyp. J., **28**(1), pp. 87–100.
[5] 2024, "Aerospace Additive Manufacturing Market by Platform," IMARC Group. Impactful Insights, Uttar Pradesh, India, Report No. SR112024A6925.
[6] Altıparmak, S. C., and Xiao, B., 2021, "A Market Assessment of Additive Manufacturing Potential for the Aerospace Industry," J. Manuf. Process., **68**, pp. 728–738.
[7] Calignano, F., Manfredi, D., Ambrosio, E. P., Biamino, S., Lombardi, M., Atzeni, E., Salmi, A., Minetola, P., Iuliano, L., and Fino, P., 2017, "Overview on Additive Manufacturing Technologies," Proc. IEEE, **105**(4), pp. 593–612.
[8] Diegel, O., Nordin, A., and Motte, D., 2019, *A Practical Guide to Design for Additive Manufacturing*, Springer Singapore.
[9] Brighenti, R., Cosma, M. P., Marsavina, L., Spagnoli, A., and Terzano, M., 2021, "Laser-Based Additively Manufactured Polymers: A Review on Processes and Mechanical Models," J. Mater. Sci., **56**(2), pp. 961–998.
[10] Verified Market Reports, 2023, "Global DMLS 3D Printing Market By Type," Verified Market Reports, Washington, DC, Report No. 870516.
[11] Jerry Underwood, A. N., 2021, "GE Aviation's Auburn Plant Ships 100,000th 3D-Printed Fuel Nozzle," Alabama, accessed Feb. 20, 2025, https://alabamanewscenter.com/2021/08/17/ge-aviations-auburn-plant-ships-100000th-3d-printed-fuel-nozzle/
[12] GE Aviation, 2020, "Next Gen: How Young Engineers Helped Bring 3D Printing to the World's Largest Jet Engine," GE Aviation, OH, accessed Feb. 20, 2025, https://blog.geaviation.com/manufacturing/next-gen-how-young-engineers-helped-bring-3d-printing-to-the-worlds-largest-jet-engine/
[13] Rolls-Royce, 2018, "3-D Printed Parts and New Materials Help Rolls-Royce to Engine Test Success," London, UK, accessed Feb. 20, 2025, https://www.rolls-royce.com/media/press-releases/2018/11-10-2018-3-d-printed-parts-and-new-materials-help-rolls-royce-to-engine-test-success.aspx
[14] Siemens, 2018, "Additive Manufacturing: Siemens Uses Innovative Technology to Produce Gas Turbines," Siemens, Munich, Germany, accessed Feb. 20, 2025, https://press.siemens.com/global/en/feature/additive-manufacturing-siemens-uses-innovative-technology-produce-gas-turbines
[15] Pratt & Whitney, 2020, "Pratt & Whitney Announces First-in-MRO Application of 3D Printing for Aero-Engine Component," Pratt & Whitney, East Hartford, CT, accessed Feb. 20, 2025, https://newsroom.prattwhitney.com/news?item=123353
[16] Sierra Turbines, 2020, "3D Printed Turbine Combines 61 Parts Into One," Sierra Turbines, San Jose, CA, accessed Feb. 20, 2025, https://www.sierraturbines.com/press/2021/1/29/3d-printed-turbine-combines-61-parts-into-one
[17] Monash University, 2019, "World's First 3D Printed Jet Engine," Monash University, Australia, accessed Feb. 20, 2025, https://www.monash.edu/mcam/news/articles/worlds-first-3d-printed-jet-engine
[18] Harvard Business School, 2016, "Additive Manufacturing Revolutionizes Aerospace," Harvard Business School, Boston, MA, accessed Feb. 20, 2025, https://digital.hbs.edu/platform-rctom/submission/additive-manufacturing-revolutionizes-aerospace/#
[19] FlightGlobal, 2021, "Pratt & Whitney's GatorWorks to 3D Print Entire Jet Engine," FlightGlobal, Sutton, UK, accessed Feb. 20, 2025, https://www.flightglobal.com/fixed-wing/pratt-and-whitneys-gatorworks-to-3d-print-entire-jet-engine/145813.article
[20] VIAM, 2020, "The Flight Test of the First Russian Small Gas Turbine MGTD-20," Moscow, Russia, accessed Feb. 20, 2025, https://viam.ru/news/7174
[21] Badum, L., Leizeronok, B., and Cukurel, B., 2021, "New Insights From Conceptual Design of an Additive Manufactured 300 W Microgas Turbine Toward Unmanned Aerial Vehicle Applications," ASME J. Eng. Gas Turbine Power, **143**(2), p. 021006.
[22] Badum, L., Prochaska, T., Schwentenwein, M., and Cukurel, B., 2024, "Ceramic and Metal Additive Manufacturing of Monolithic Rotors From SiAlON and Inconel and Comparison of Aerodynamic Performance for 300W Scale Microturbines," ASME J. Eng. Gas Turbine Power, **146**(2), p. 021006.
[23] Badum, L., and Cukurel, B., 2024, "Multidisciplinary Design Methodology for Micro-Gas-Turbines—Part II: System Analysis and Optimization," ASME J. Eng. Gas Turbine Power, **146**(10), p. 101002.
[24] Badum, L., Schirrecker, F., and Cukurel, B., 2024, "Multidisciplinary Design Methodology for Micro-Gas-Turbines—Part I: Reduced Order Component Design and Modeling," ASME J. Eng. Gas Turbine Power, **146**(10), p. 101001.
[25] Çelik, A., Linsky, D., Miezner, R., Kleiman, A., Leizeronok, B., Palman, M., Acarer, S., and Cukurel, B., 2022, "Design Methodology and Concept Demonstration of Preassembled Additively Manufactured Turbomachinery Systems: Case Study of Turbocharger Based Medical Ventilators," ASME J. Eng. Gas Turbine Power, **144**(12), p. 121010.
[26] ASTM Committee F42, 2022, "Standard Guide for Additive Manufacturing—Design—Post-Processing for Metal PBF-LB," ASTM, PA, Standard No. F3530-22.
[27] Li, R., Liu, J., Shi, Y., Wang, L., and Jiang, W., 2012, "Balling Behavior of Stainless Steel and Nickel Powder During Selective Laser Melting Process," Int. J. Adv. Manuf. Technol., **59**(9–12), pp. 1025–1035.
[28] Sola, A., and Nouri, A., 2019, "Microstructural Porosity in Additive Manufacturing: The Formation and Detection of Pores in Metal Parts Fabricated by Powder Bed Fusion," J. Adv. Manuf. Process., **1**(3).
[29] Khairallah, S. A., Anderson, A. T., Rubenchik, A., and King, W. E., 2016, "Laser Powder-Bed Fusion Additive Manufacturing: Physics of Complex Melt Flow and Formation Mechanisms of Pores, Spatter, and Denudation Zones," Acta Mater., **108**, pp. 36–45.
[30] Kruth, J. P., Froyen, L., Van Vaerenbergh, J., Mercelis, P., Rombouts, M., and Lauwers, B., 2004, "Selective Laser Melting of Iron-Based Powder," J. Mater. Process. Technol., **149**(1–3), pp. 616–622.
[31] Mohr, G., Altenburg, S. J., Ulbricht, A., Heinrich, P., Baum, D., Maierhofer, C., and Hilgenberg, K., 2020, "In-Situ Defect Detection in Laser Powder Bed Fusion by Using Thermography and Optical Tomography—Comparison to Computed Tomography," Metals (Basel), **10**(1), p. 103.
[32] Manfredi, D., Calignano, F., Krishnan, M., Canali, R., Paola, E., Biamino, S., Ugues, D., Pavese, M., and Fino, P., 2014, "Additive Manufacturing of Al Alloys and Aluminium Matrix Composites (AMCs)," *Light Metal Alloys Applications*, W. A. Monteiro, ed., InTechOpen, Rijeka, pp. 1–32.
[33] Snyder, J. C., and Thole, K. A., 2020, "Understanding Laser Powder Bed Fusion Surface Roughness," J. Manuf. Sci. Eng., **142**(7), p. 071003.
[34] Gibson, I., Rosen, D., and Stucker, B., 2015, *Additive Manufacturing Technologies*, Springer, New York.
[35] García-Contreras, R., Romero Gutiérrez, A., Armas, O., and Herreros, J. M., 2024, "Fuel Lubricity Assessment of Fossil and Synthetic Paraffinic Kerosene to Be Used in Reciprocating Engines," Energy Fuels, **38**(19), pp. 18652–18659.
[36] Mujeebu, M. A., Abdullah, M. Z., Bakar, M. Z. A., Mohamad, A. A., and Abdullah, M. K., 2009, "Applications of Porous Media Combustion Technology – A Review," Appl. Energy, **86**(9), pp. 1365–1375.
[37] Saravanamuttoo, H. I. H., Cohen, H., Rogers, G. F. C., Nix, A. C., and Straznicky, P. V., 2017, *Gas Turbine Theory*, Pearson, London, UK.
[38] High Temp Metals, 2024, "Inconel 722 Tech Data," High Temp Metals, Sylmar, CA, accessed Oct. 30, https://www.hightempmetals.com/techdata/hitempInconel722data.php
[39] Brian Rowe, W., 2012, *Hydrostatic, Aerostatic and Hybrid Bearing Design*, Elsevier, Amsterdam, The Netherlands.
[40] Dietrich, B., Schabel, W., Kind, M., and Martin, H., 2009, "Pressure Drop Measurements of Ceramic Sponges—Determining the Hydraulic Diameter," Chem. Eng. Sci., **64**(16), pp. 3633–3640.
[41] Dixon, S. L., and Hall, C. A., 2014, *Fluid Mechanics and Thermodynamics of Turbomachinery*, Elsevier, Amsterdam, The Netherlands.
[42] Khatami, F. S. R., Safavisohi, B., and Sharbati, E., 2007, "Porosity and Permeability Effects on Centerline Temperature Distributions, Peak Flame Temperature, Flame Structure, and Preheating Mechanism for Combustion in Porous Media," ASME J. Energy Resour. Technol., **129**(1), pp. 54–65.
[43] Bell, I. H., Wronski, J., Quoilin, S., and Lemort, V., 2014, "Pure and Pseudo-Pure Fluid Thermophysical Property Evaluation and the Open-Source Thermophysical Property Library CoolProp," Ind. Eng. Chem. Res., **53**(6), pp. 2498–2508.
[44] Ergin, C. C., Verstraete, T., and Saracoglu, B. H., 2024, "The Design and Optimization of Additively Manufactured Radial Compressor of a Miniature Gas Turbine Engine," ASME J. Fluids Eng., **146**(7), p. 071108.
[45] Châtel, A., and Verstraete, T., 2023, "Multidisciplinary Optimization of the SRV2-O Radial Compressor Using an Adjoint-Based Approach," Struct. Multidiscip. Optim., **66**(5), p. 112.

[46] Verstraete, T., 2010, "CADO: A Computer Aided Design and Optimization Tool for Turbomachinery Applications," Second International Conference on Engineering Optimization, Lisabon, Portugal, Sept. 6–9, accessed Feb. 21, 2025, https://api.semanticscholar.org/CorpusID:35829990.
[47] Mueller, L., and Verstraete, T., 2019, "Adjoint-Based Multi-Point and Multi-Objective Optimization of a Turbocharger Radial Turbine," Int. J. Turbomach., Propul. Power, **4**(2), p. 10.
[48] Schwalbach, M., Verstraete, T., Müller, L. R., and Gauger, N., 2018, "CAD-Based Adjoint Multidisciplinary Optimization of a Radial Turbine Under Structural Constraints," Global Power and Propulsion Forum, Global Power & Propulsion Society, Montreal, May 7–9, Paper No. GPPS-NA-2018-133, accessed Feb. 21, 2025, https://api.semanticscholar.org/CorpusID:189806860
[49] Schwalbach, M., 2021, "An Efficient CAD-Based Multidisciplinary Optimization Framework for Turbomachinery Design," Ph.D. thesis, Technische Universität Kaiserslautern, Kaiserslautern, Germany.
[50] EOS GmbH – Electro Optical Systems, n.d., "EOS NickelAlloy IN718 Material Data Sheet Metal Solutions," Krailling, Germany, accessed Feb. 20, 2025, https://www.eos.info/05-datasheet-images/Assets_MDS_Metal/EOS_NickelAlloy_IN718/Material_DataSheet_EOS_NickelAlloy_IN718_en.pdf
[51] The CRECK Modeling Group, 2024, "Homepage - Creckmodeling," The CRECK Modeling Group, Milano, Italy, accessed Dec. 23, https://www.creckmodeling.polimi.it/
[52] Humer, S., Frassoldati, A., Granata, S., Faravelli, T., Ranzi, E., Seiser, R., and Seshadri, K., 2007, "Experimental and Kinetic Modeling Study of Combustion of JP-8, Its Surrogates and Reference Components in Laminar Nonpremixed Flows," Proc. Combust. Inst., **31**(1), pp. 393–400.
[53] Brian Rowe, W., 2012, *Hydrostatic, Aerostatic, and Hybrid Bearing Design*, Butterworth-Heinemann, Waltham, MA.
[54] IRD Balancing, 2009, *Balance Quality Requirements of Rigid Rotors - The Practical Application of ISO 1940/1*, IRD Balancing, Louisville, KY.
[55] Guo, Z., Hirano, T., and Kirk, R. G., 2005, "Application of CFD Analysis for Rotating Machinery—Part I: Hydrodynamic, Hydrostatic Bearings and Squeeze Film Damper," ASME J. Eng. Gas Turbine Power, **127**(2), pp. 445–451.
[56] AEA Technology, 2001, "CFX-TASCflow 2.11.1 Documentation," AEA Technology, Ontario, Canada.
[57] Kirk, R. G., Raju, K. V. S., and Ramesh, K., 1999, "PC-Based Analysis of Turbomachinery Vibration," Shock Vib. Digest., **31**(6), pp. 449–454.
[58] Fang, Z.-C., Wu, Z.-L., Huang, C.-G., and Wu, C.-W., 2020, "Review on Residual Stress in Selective Laser Melting Additive Manufacturing of Alloy Parts," Opt. Laser Technol., **129**, p. 106283.
[59] Pant, P., Proper, S., Luzin, V., Sjöström, S., Simonsson, K., Moverare, J., Hosseini, S., Pacheco, V., and Peng, R. L., 2020, "Mapping of Residual Stresses in As-Built Inconel 718 Fabricated by Laser Powder Bed Fusion: A Neutron Diffraction Study of Build Orientation Influence on Residual Stresses," Addit. Manuf., **36**, p. 101501.
[60] Arif, Z. U., Khalid, M. Y., and Rehman, E. U., 2022, "Laser-Aided Additive Manufacturing of High Entropy Alloys: Processes, Properties, and Emerging Applications," J. Manuf. Process., **78**, pp. 131–171.
[61] Qu, A., and Li, F., 2023, "Effect of Double Crack on Fatigue Crack Growth Life of 3D Printing Compressor Impeller," Thin-Walled Struct., **189**, p. 110883.
[62] Mehmert, P., 2023, "Residual Stress Analysis and Geometrical Tolerances in Powder Bed Fusion and Direct Energy Deposition Processes," *Quality Analysis of Additively Manufactured Metals*, Elsevier, Amsterdam, The Netherlands, pp. 429–486.
[63] Singh, U. P., Swaminathan, S., and Phanikumar, G., 2022, "Thermo-Mechanical Approach to Study the Residual Stress Evolution in Part-Scale Component During Laser Additive Manufacturing of Alloy 718," Mater. Des., **222**, p. 111048.
[64] Mukherjee, T., Zhang, W., and DebRoy, T., 2017, "An Improved Prediction of Residual Stresses and Distortion in Additive Manufacturing," Comput. Mater. Sci., **126**, pp. 360–372.